



OPEN

Titania nanotubes with aminated reduced graphene oxide as efficient photocatalysts for antibacterial application under visible light

Kyoung-Suk Moon¹, Ji-Myung Bae¹, Eun-Joo Choi^{2,3} & Seunghan Oh^{1,3}✉

Titania and reduced graphene oxide (rGO) are well-known materials with excellent photocatalytic properties, but research on the photocatalytic-based antibacterial effects of their combination remains limited. This study explored the suitability of titania nanotubes (TiO_2 NTs) combined with rGO and two terminal functional groups (nonfunctional and aminated groups (NH_2)) as efficient photocatalysts for antimicrobial applications under visible light irradiation. Field-emission scanning electron microscopy observations revealed that rGO covered the entire surface of the TiO_2 NTs. Tauc plots calculated from the spectra of diffuse reflectance spectroscopy showed that the band gaps of the nonfunctional and amine functional groups of rGO-coated TiO_2 NTs were 2.40 and 2.21 eV, respectively. Therefore, all rGO-coated TiO_2 NTs exhibited photocatalytic activity under 470 nm visible light irradiation. An antibacterial colony forming unit test using *S. aureus* and *P. aeruginosa*, and two enzymatic activity tests (superoxide dismutase and catalase) on the same bacteria, showed that the aminated rGO-coated TiO_2 NTs showed excellent antibacterial activity under 470 nm visible-light irradiation compared to nonfunctional rGO-coated TiO_2 NTs and uncoated TiO_2 NTs groups. In addition, the MTT assay showed that the aminated rGO-coated TiO_2 NTs enhanced cell viability after visible light irradiation. Therefore, the combination of aminated rGO-coated TiO_2 NTs and visible-light-triggered photocatalytic activity has significant potential for expressing antibacterial properties in dental applications.

Keywords Photocatalytic effect, Reduced graphene oxide, Titania nanotubes, Visible light, Antibacterial activity

Dental implants are widely used as an effective tool to address tooth deficiencies. However, the successful retention of dental implants is affected by various factors. Bacterial infection is one of the leading causes of implant failure^{1,2}. Bacterial infections are primarily associated with an imbalance in the oral microbiome, which can damage the bone tissue surrounding the implant, ultimately leading to implant failure^{3,4}. Peri-implantitis is the inflammation of the tissue surrounding an implant and is often caused by various pathogenic bacteria. This inflammation occurs as bacteria adhere to the implant surface and can lead to loss of alveolar bone around the implant^{5,6}. Studies have shown that the inflammatory response is modulated continuously by oral bacteria, which emphasizes the need for continuous antibiotic treatment⁷. Additionally, the ongoing struggle against pathogenic bacteria and the threat of antibiotic resistance have resulted in a strong academic interest in alternative antibacterial strategies.

Photocatalysis, particularly involving titanium dioxide (TiO_2), has shown great promise for continuous water treatment and organic compound removal owing to its oxidative solid abilities and long-term functionality. However, its activation under ultraviolet (UV) light limits its practical application in the medical field because of the potential health hazards associated with UV exposure in the human body. Consequently, extending the photocatalytic response of TiO_2 to the visible light spectrum has become an important goal for utilizing Ti-based dental implant materials^{8,9}.

It was previously reported that a combination of noble metal nanoparticles and titania nanotubes prepared on Ti implant surfaces showed antibacterial activity that was triggered by visible light irradiation^{10,11}. However, a lack of cell adhesion owing to the hydrophobic nature of the noble metal did not improve the osteogenic

¹Department of Dental Biomaterials and the Institute of Biomaterial and Implant, Wonkwang University College of Dentistry, Iksan-Daero 460, Iksan 54538, Republic of Korea. ²Department of Oral and Maxillofacial Surgery, Wonkwang University College of Dentistry, Iksan-Daero 460, Iksan 54538, Republic of Korea. ³Eun-Joo Choi and Seunghan Oh have contributed equally to this work. ✉email: shoh@wku.ac.kr

performance. In addition, using noble metal nanoparticles as stepping stones between the valence and conduction bands of TiO_2 to increase the photocatalytic efficacy under visible light can also improve the visible light-mediated photocatalytic efficacy. However, it is difficult to expect fundamental improvements in the photocatalytic efficacy owing to the limited space utilization of the stepping stones. Therefore, it is necessary to discover new materials that can overcome the hydrophobicity of noble metals and exhibit robust photocatalytic activity under visible light when combined with titania.

Reduced graphene oxide (rGO) is a material in which the oxygen content is reduced in graphene oxide (GO), resulting in high conductivity and a variety of physicochemical properties¹². rGO is a promising photocatalyst for water treatment and antibiotic degradation, owing to its semiconductive properties^{13,14}. In addition, it is partly hydrophilic because of the presence of residual hydroxyl groups after the reduction process. The degree of hydrophilicity can be controlled by attaching various hydrophilic end groups^{15,16}. The presence of aminated and carboxylated surfaces in reduced graphene oxide (rGO) enhances hydrophilicity, thereby resulting in increased chemical reactivity. These functional groups can enhance adhesion and interaction between cells, thus facilitating cellular attachment and spreading. Further, at physiological pH, an aminated surface carries a positive charge that readily attracts negatively charged molecules such as most proteins, resulting in the promotion of cell attachment, proliferation, and osteogenic differentiation compared to a carboxylated surface, which has a negative charge that interacts with only some positively charged molecules^{17,18}. Therefore, we selected an aminated rGO surface over a carboxylated rGO surface in this study.

In addition, the antimicrobial activity of rGO is mainly attributed to its unique nanostructure and physicochemical properties. rGOs can cause physical damage to bacterial cell membranes, disrupting their physiological functions, and eventually leading to their death^{19,20}. Many studies have also reported the visible-light-mediated photocatalytic activity of a combination of rGO and TiO_2 for dye sensitization and organic compound degradation^{21–23}. Therefore, the authors predicted that rGO, with its tunable hydrophilicity and inherent photocatalytic potency, is the most appropriate candidate for maximizing visible light-mediated photocatalytic potency and biocompatibility through its combination with TiO_2 .

In this study, the structural features and antibacterial efficacy of this novel rGO-TiO₂ NTs combination were evaluated under visible light conditions. The methods by which different functional groups of rGO influence the photocatalytic mechanisms and antibacterial outcomes were investigated, and the dynamics between the unique structural attributes of the rGO-TiO₂ NTs combination and their performance were analyzed.

Materials and methods

Preparation and characterization of rGO-coated TiO₂ NTs (rGO-TiO₂ NTs)

TiO₂ NTs (diameter: 100 nm) were prepared by anodizing (voltage: 20 V, duration: 30 min) a pure Ti sheet (99.5%; size: 5 × 5 cm², thickness: 250 μm; Hyundai Titanium Co., Incheon, South Korea) in a hydrofluoric acid (0.5 w/v%, Merck & Co., Chicago, IL, USA) solution. The anodized specimen was heat-treated (temperature: 500 °C, soaking time: 2 h) to crystallize the specimen. Two rGO powders including (1) a non-functional rGO (NON-rGO) and (2) an aminated rGO ($\text{NH}_2\text{-rGO}$) (Sigma-Aldrich Co., St. Louis, MO, USA) were used in this study. The rGO powder coating on the surface of the TiO₂ NTs specimen was fabricated using electrophoretic deposition (EPD)²⁴. The rGO powder was dispersed in deionized water (concentration: 0.5 mg/mL) by ultrasonication (VC 505, Sonics & Materials Inc., Newtown, CT, USA) with magnesium nitrate hydrate (concentration: 0.05 mg/mL: Mg(NO₃)₂·6H₂O, Sigma-Aldrich Co., St Louis, MO, USA) to activate the charge on the rGO surface. rGO dispersed in deionized water was coated onto the TiO₂ NTs via EPD for 1 min (EPD voltage: 50 V). After the EPD process, the rGO-TiO₂ NTs specimens were washed and dried at 60 °C for 24 h. The rGO-TiO₂ NTs were characterized using field-emission scanning electron microscopy (FE-SEM; S-4800; Hitachi Co., Tokyo, Japan), contact angle measurements, diffuse reflectance ultraviolet-visible-near infrared spectrophotometry (DRS; SolidSpec-3700; Shimadzu Co., Kyoto, Japan), and Photoluminescence spectrophotometry (PL; LabRAM HR-800, Horiba Co., Kyoto, Japan). The optical band gap energy of the rGO-TiO₂ NTs was determined using the Tauc plot calculated from the DRS spectra as shown in Eq. (1)²⁵.

$$(\alpha h\nu)^{1/n} = A (h\nu - E_g), \quad (1)$$

where α , $h\nu$, A , and E_g are the absorption coefficient, incident light frequency, proportionality constant and band gap, respectively. The value of the exponent 'n' determines the nature of the electronic transition; further, the anatase TiO₂ and rGO typically exhibit an indirect band gap, and hence, the exponent value corresponds to 2^{26,27}. From the Tauc plot, the linear extrapolation of $(\alpha h\nu)^{1/n}$ to the zero of the Y-axis provides the value of the optical band gap energy of the specimen.

Methylene blue degradation test

Methylene blue (MB) degradation tests were performed to evaluate the photocatalytic activity of the rGO-TiO₂ NTs under visible light at 470 nm. The experimental specimen was placed in a 12-well plate and 1 mL of methylene blue (MB) solution (1 ppm) was added to each well. Lab-fabricated 470 nm LED lights with a power density of 5.5 mW/cm² were irradiated on the specimens for 15 and 30 min. The distance between the specimen and the LED was 4 cm. The absorbance of the MB solution in the experimental groups was determined using a UV-vis spectrometer (wavelength of maximum absorbance peak = 665 nm; UVmini-1240, Shimadzu Co., Kyoto, Japan).

In vitro biocompatibility test

Live/dead and MTT assays were performed to test the in vitro biocompatibility of the rGO-TiO₂ NTs. Human mesenchymal stem cells (hMSCs Lonza Co., Basel, Switzerland) were cultured in an α-modified Eagle's minimum essential medium (α-MEM; Invitrogen Co., Carlsbad, CA, USA) supplemented with 10% fetal bovine serum (FBS; Invitrogen) and 1% antibiotics (Invitrogen). To perform the live/dead assay, hMSCs were dispensed into a 24-well plate (concentration = 1×10^4 cells/well) including the specimen. After 24 h of incubation, 470 nm visible light was irradiated to the specimen for 15 min (Fig. 1). After an additional 24 h of incubation, 500 μL of phosphate buffer solution (PBS; Invitrogen) including 2 μM of calcein AM (live cell staining agent; Invitrogen) and 4 μM of ethidium homodimer-1 (dead cell staining agent; Invitrogen) was added to the well. After staining for 30 min, live (green) and dead (red) cells were visually inspected using an inverted fluorescence microscope (CKX41; Olympus Co., Tokyo, Japan).

An MTT assay kit (Sigma-Aldrich, St Louis, MO, USA) was used to evaluate initial cell metabolic activity, including survival and growth. The cell culture, light irradiation conditions, and procedure in the MTT assay were the same as those in the live-dead assay. After an additional 24 h of incubation, 100 μg/mL of MTT solution was added to each well, and the specimens were cultured at 37 °C in a 5% CO₂ incubator. After 4 h of MTT treatment, DMSO (Sigma-Aldrich, St Louis, MO, USA) was added to each well to dissolve the formazan produced by the MTT solution. The absorbance of the final solution was measured at 570 nm using a microplate reader (SpectraMax Mini; Molecular Devices Co., Sunnyvale, CA, USA).

Colony forming unit test

Colony forming unit (CFU) tests against *Staphylococcus aureus* (*S. aureus*; ATCC 25,923, Manassas, VA, USA) and *Pseudomonas aeruginosa* (*P. aeruginosa*; PA14²⁸) were conducted to estimate the photocatalysis-based antimicrobial activities of the two rGO TiO₂ NTs. After 24 h of initial incubation of the bacterial strains in fresh media, the bacterial solution (500 μL) was adjusted to a concentration of 1×10^5 CFU/mL. The solution with the adjusted concentration was inoculated onto specimens (1 × 1 cm). After an additional 24 h of incubation, the specimen was exposed to 470 nm visible light for 15 min. Then, the bacteria on the specimen were collected and diluted in 100 μL of PBS solution. The PBS solution, including bacteria, was placed on an agar plate (100 mm in diameter) and incubated for 24 h at 37 °C. After 24 h of incubation, a visual inspection was performed to analyze the resulting CFU values.

Enzymatic activity analysis

The enzymatic activities of superoxide dismutase (SOD) and catalase (CAT) in *S. aureus* and *P. aeruginosa* were measured to evaluate the antimicrobial capabilities of the rGO-TiO₂ NTs under visible light irradiation at 470 nm. The detailed procedure for extracting these enzymes from bacteria is described in previous studies²⁹. The cultivation and inoculation concentrations of the bacteria as well as other experimental conditions were the same as those used for the CFU test. To elaborate on the experimental procedures for the SOD and CAT enzymatic activity assays, after visible light irradiation, the bacteria collected from each specimen were centrifuged (at 5,000 rpm for 10 min) and washed with PBS. The washed bacteria were then sonicated (Sonics VCX-130, USA) for 20 s (with 5-s treatment and 3-s intervals). The supernatant was collected from the sonicated solution including bacteria by further centrifugation (at 12,000 rpm for 20 min at 4 °C) and was then utilized for SOD (EIASODC, Invitrogen Co., Carlsbad, CA, USA) and CAT (CAT 100, Sigma-Aldrich, St. Louis, MO, USA) enzymatic activity assays. The absorbance at 450 and 570 nm was measured using a microplate reader (SpectraMax Mini), and the results were calculated according to a standard calibration curve. The Bradford reagent (Sigma-Aldrich, St. Louis, MO, USA) was used to measure the protein concentrations. Owing to the limited number of bacteria cultured on one specimen, bacteria extracted from two specimens were used to obtain one sample.

Statistical analysis

One-way analysis of variance (IBM SPSS Statistics 24.0; IBM, USA) and post hoc Games-Howell tests were used to perform the statistical analysis. All data are expressed as the mean ± standard deviation. Differences were considered statistically significant at $p < 0.05$.

Results

Figure 2 shows plain and oblique FE-SEM images of the NON-rGO and NH₂-rGO groups. Both rGO-TiO₂ groups showed a uniform thin coating of rGO layer onto the surface of TiO₂ NTs, and no significant differences

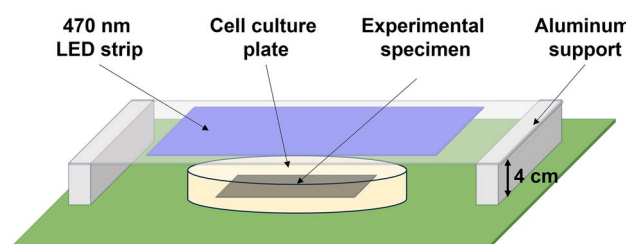


Fig. 1. Schematic diagram of 470 nm light emitting diode (LED) irradiation system for in vitro test.

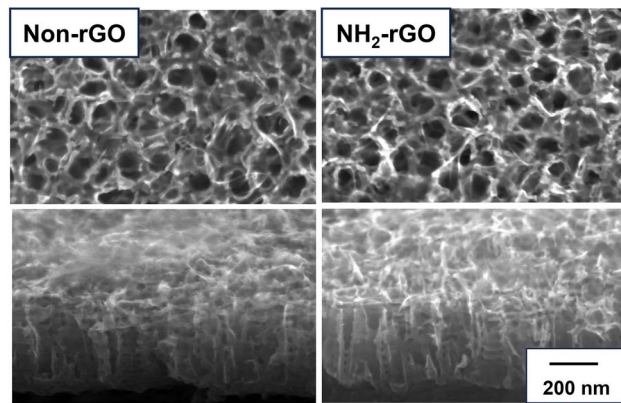


Fig. 2. (A) FE-SEM images (plain and oblique views: $\times 100,000$) of NON-rGO and NH₂-rGO for 1 min coating.

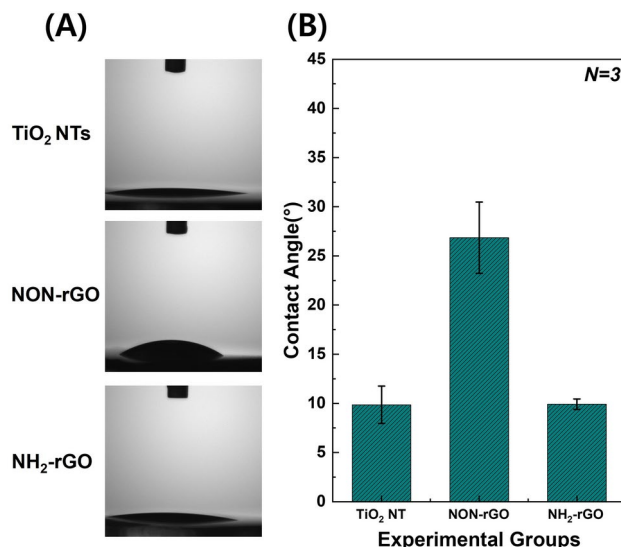


Fig. 3. (A) Contact angle measurement images and (B) results of TiO₂ NTs, NON-rGO, and NH₂-rGO groups for 1 min coating.

were observed in surface geometry between the two experimental groups. In Fig. 3, the results of the contact angle measurements indicate that all rGO-TiO₂ NTs specimens were hydrophilic, but the contact angle of the non-rGO specimens was higher than that of the other groups.

Figure 4 shows the diffuse reflectance UV – Vis – NIR spectra and band gap energies of the TiO₂ NTs, NON-rGO, and NH₂-rGO groups. The band gap energies of the TiO₂ NTs, NON-rGO-TiO₂ NTs, and NH₂-rGO-TiO₂ NTs groups were 3.20, 2.40, and 2.21 eV, respectively. These band gap energies correspond to light wavelengths of 387.5, 516.7, and 561 nm. Therefore, both rGO-TiO₂ NTs groups were confirmed to exhibit photocatalytic reactions to visible light irradiation at 470 nm, which is the wavelength used in this study. The results of the PL spectrophotometry (Fig. 5) indicated that the PL intensities of both the NON-rGO and NH₂-rGO groups were lower than those of the TiO₂ NTs (control). The PL data represents the excited state of the photocatalytic semiconductor material affected by the recombination of photogenerated charges (e⁻ and h⁺), so a lower PL intensity indicates better charge separation of e⁻ and h⁺ and more powerful photocatalytic effect³⁰.

Figure 6 shows the degradation values of MB dye by the TiO₂ NTs, NON-rGO, and NH₂-rGO groups after 15 and 30 min of visible light irradiation at 470 nm. The MB degradation in the NON-rGO and NH₂-rGO groups decreased faster than that in the TiO₂ NTs, and there was no significant difference in MB degradation between the two rGO groups.

Figure 7 shows the calcein AM- and EthD-1-stained fluorescent images and the results of the MTT assay for the experimental groups. There were no damaged or dead cells (red fluorescence) in any of the experimental groups under 470 nm visible light irradiation. From the results of the MTT assays (Fig. 7B), the cell viability of hMSCs cultured in NH₂-rGO specimens tended to increase after visible light irradiation, whereas the TiO₂ NTs and NON-rGO groups showed the opposite results. Although the cell viability value of the NON-rGO

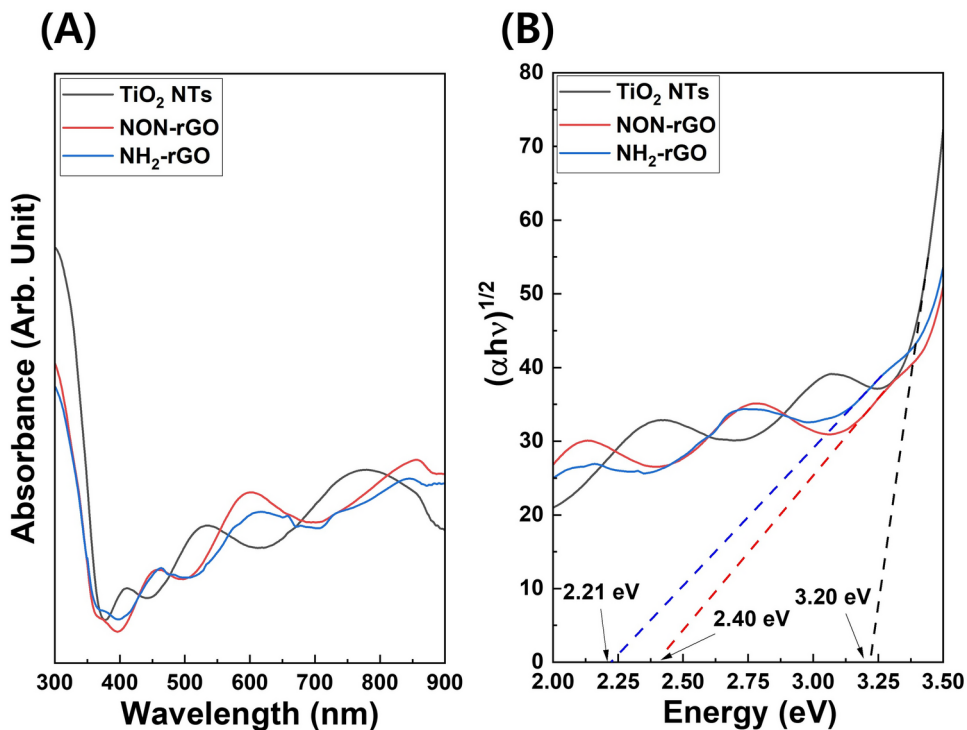


Fig. 4. (A) Diffuse reflectance UV–Vis–NIR spectra, and (B) Tauc plot of TiO_2 NTs, NON-rGO, and NH_2 -rGO groups.

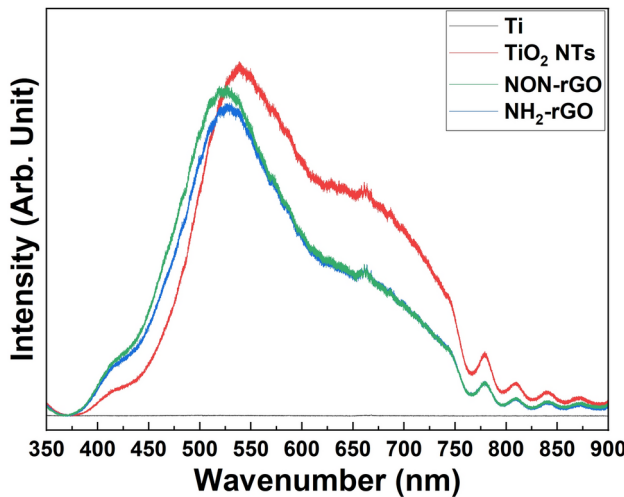


Fig. 5. Photoluminescence (PL) spectra of TiO_2 NTs, NON-rGO, and NH_2 -rGO groups.

specimens was significantly lower than that of TiO_2 NTs and NH_2 -rGO specimens, regardless of visible light irradiation, it was still above the minimum standard of 70% for biocompatibility specified in ISO 10,993-5¹⁷. Therefore, the results of the MTT assay confirmed that all the experimental groups were biocompatible.

Figure 8 shows the images and CFU values of *S. aureus* and *P. aeruginosa* tested in this study. Visible light irradiation reduced the CFU values of all experimental groups, especially the NH_2 -rGO group, which showed a statistically significant reduction in the CFU values for both bacteria ($p < 0.05$).

Figure 9 shows the superoxide dismutase (SOD) enzymatic activities of *S. aureus* and *P. aeruginosa*. Under the experimental conditions of *S. aureus*, the SOD activity values of the NON-rGO and NH_2 -rGO groups after visible light irradiation were significantly reduced ($p < 0.05$). In addition, under the experimental conditions for *P. aeruginosa*, the SOD activity values of all experimental groups tended to decrease after visible light irradiation. Also, the value of NH_2 -rGO was reduced significantly ($p < 0.05$).

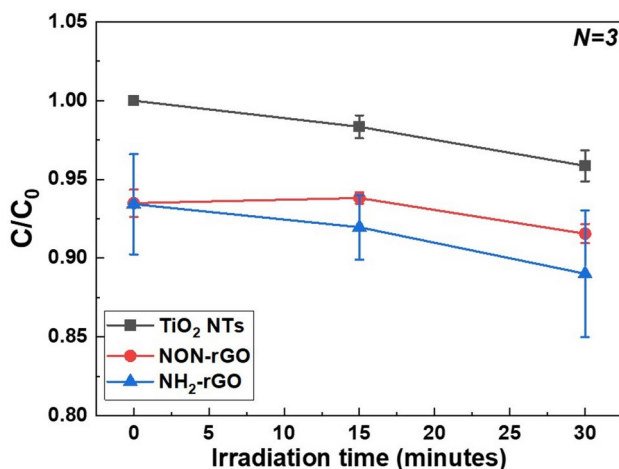


Fig. 6. Degradation plot of methylene blue (MB) dye of TiO₂ NTs, NON-rGO, and NH₂-rGO groups. under 470 nm visible light irradiation.

Figure 10 illustrates the catalase (CAT) enzymatic activities of *S. aureus* and *P. aeruginosa* tested in this study. Under the experimental conditions for *S. aureus*, the CAT enzyme activity of all experimental groups did not show any significant reduction after visible light irradiation ($P > 0.05$). However, under the experimental conditions for *P. aeruginosa*, only the SOD activity value of NH₂-rGO group was significantly reduced after visible light irradiation compared to the other experimental groups ($p < 0.05$).

Discussion

The main objectives of this study were to (1) characterize the surface of rGO-coated TiO₂ NTs to evaluate whether the presence of rGO affects the visible light-mediated photocatalytic activity of TiO₂ NTs and (2) investigate the antibacterial activity of both NON-rGO-coated TiO₂ NTs and NH₂-rGO-coated TiO₂ NTs under visible light at 470 nm, to analyze whether the presence of the terminal functional group of rGO affects the antibacterial activity and biocompatibility of TiO₂ NTs.

The antibacterial mechanism used in this study was a visible light-mediated photocatalytic effect based on the combination of rGO and TiO₂ oxide as a photocatalyst. TiO₂ only exhibits photocatalytic effects under UV light owing to its semiconducting nature and large bandgap energy between the conduction band and valence band of TiO₂. For TiO₂ to exhibit photocatalytic effects under visible light irradiation, the large bandgap energy distance between the conduction and valence bands must be reduced. The visible light-mediated photocatalytic activity can be achieved by coating a material such as a noble metal, heavy metal, or graphene oxide that acts as a bridge^{31–33}. Generally, to exhibit photocatalytic effects, electrons in the valence band must be excited to the conduction band by absorbing a certain amount of energy in the form of light. In this case, the noble metal nanoparticles, which do not have their own photocatalytic activity, act as a stepping stone between the valence band and the conduction band, thereby enabling the photocatalytic effect to be activated by visible light, which has lower energy than ultraviolet light. However, because the area of this stepping stone is small, only a limited number of electrons can be excited, and this results in a constrained photocatalytic effect. In contrast, rGO exerts its own photocatalytic activity¹³. Therefore, a combination of rGO and TiO₂, both of which possess their own photocatalytic activities, will result in an extensive photocatalytic activity compared to a combination of noble metal nanoparticles and TiO₂. In addition, the correlation between the photocatalytic and antimicrobial effects is driven by the role of reactive oxygen species (ROS) groups, such as hydroxyl radicals, superoxide anions, and hydrogen peroxide, generated by the photocatalytic effect, which result in damage to bacteria through lipid peroxidation, protein oxidation, and DNA damage^{34,35}. Therefore, the first objective of this study was to evaluate the photocatalytic effect of rGO-coated TiO₂ NTs under visible light through surface characterization.

The FE-SEM images shown in Fig. 2 show that the rGO nanosheets were deposited uniformly on the surface of the TiO₂ NTs. There were no significant differences in the surface geometry between the two groups. The DRS spectra and Tauc plot results demonstrate that both rGO TiO₂ NTs groups exhibited sufficient photocatalytic activity to generate ROS groups under 470 nm visible light to exhibit antimicrobial activity. Pilot tests were conducted to optimize the coating time of rGO on the surface of TiO₂ NTs for coating periods of 30 s, 1 min, 3 min, and 5 min. The FE-SEM images (Figure S1) show that the rGO sheet layer was barely observed on the TiO₂ NTs surface after a coating time of 30 s. In addition, the sheet-like rGO nanoparticles began to be stacked in multiple layers after 3 min of coating, and the rGO nanosheets were coated so thickly that the nanotube structure was not visible after 5 min of coating.

The band gap energy calculations from the Tauc plot (Figure S2 and S3) showed that the 1 min rGO-coated rGO-TiO₂ NTs groups exhibited the lowest bandgap energy and were expected to show the best photocatalytic activity among all coating periods. Unlike the single or double peaks detected in the Tauc plot of common semiconducting materials, multiple peaks were observed in the Tauc plot of this study. Previous studies related to the photocatalytic activity of TiO₂ nanotubes also observed multiple peaks in the Tauc plots, but specific

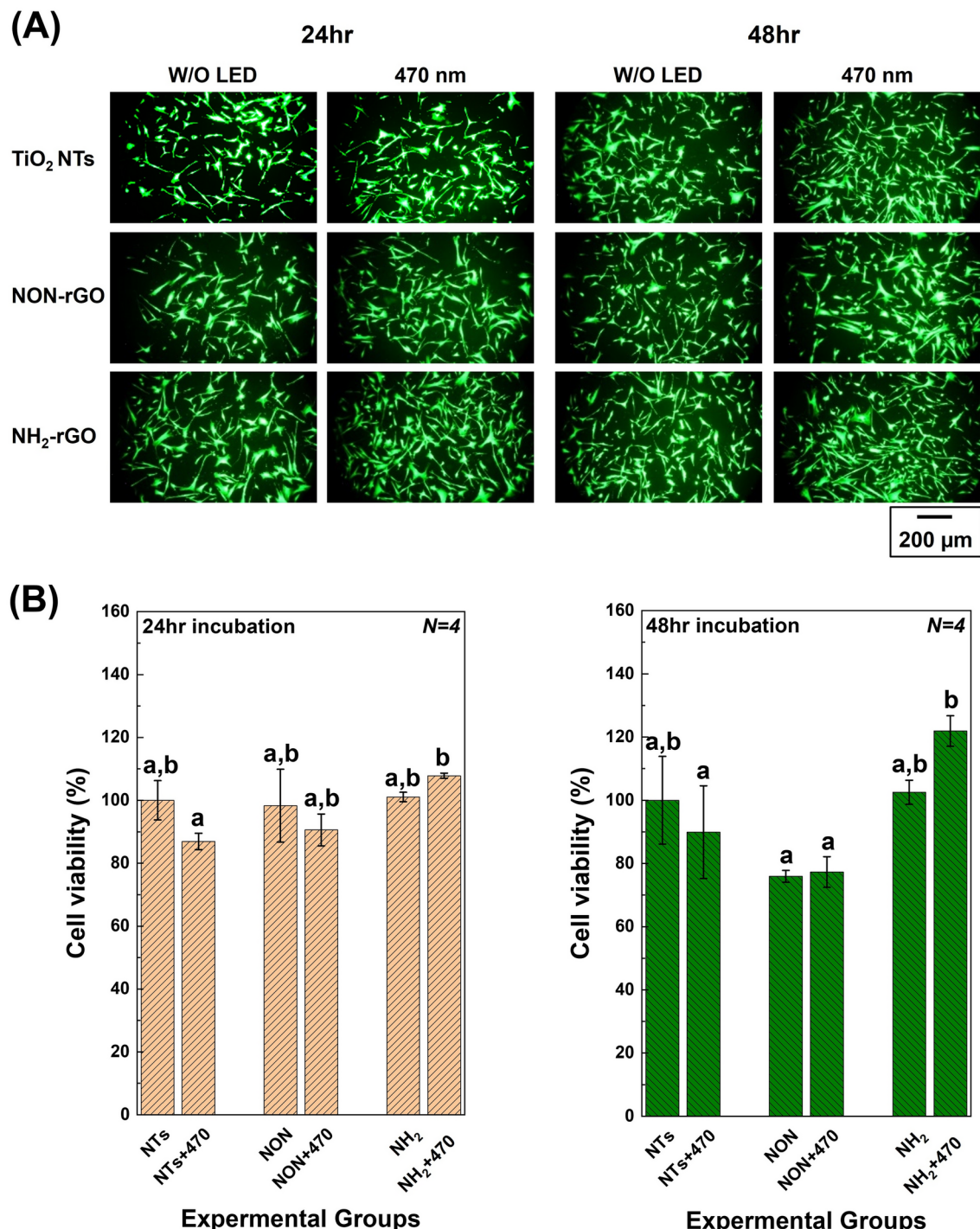


Fig. 7. (A) Calcein AM and EthD-1 (Live-Dead) stained fluorescent images and (B) MTT assay results of hMSCs on TiO₂ NTs, NON-rGO, and NH₂-rGO groups with 470 nm visible light irradiation (Different alphabetical letter means that there is significant difference between groups, $P < 0.05$).

explanations were not provided^{36–38}. We speculate that this phenomenon is caused by a unique combination of the crystalline structure of TiO₂ nanotubes. When titania nanotubes are heat-treated at 500 °C, the titania nanotubes and the base substrate change to anatase and rutile crystalline phases, respectively³⁹. Therefore, the heterojunction systems of coupled semiconductors (anatase and rutile TiO₂) may have various heterojunction structures, allowing heat-treated TiO₂ nanotubes to exhibit multiple energy levels, thus resulting in multiple peaks in the Tauc plot^{40,41}. Additionally, among the multiple peaks in the Tauc plot, the main peak at the higher energy level (shortest wavelength) corresponds to the optical gap, while the other peaks at lower energy levels (longer wavelengths) correspond to the fundamental gaps of the semiconductor^{42,43}. Consequently, in this study,

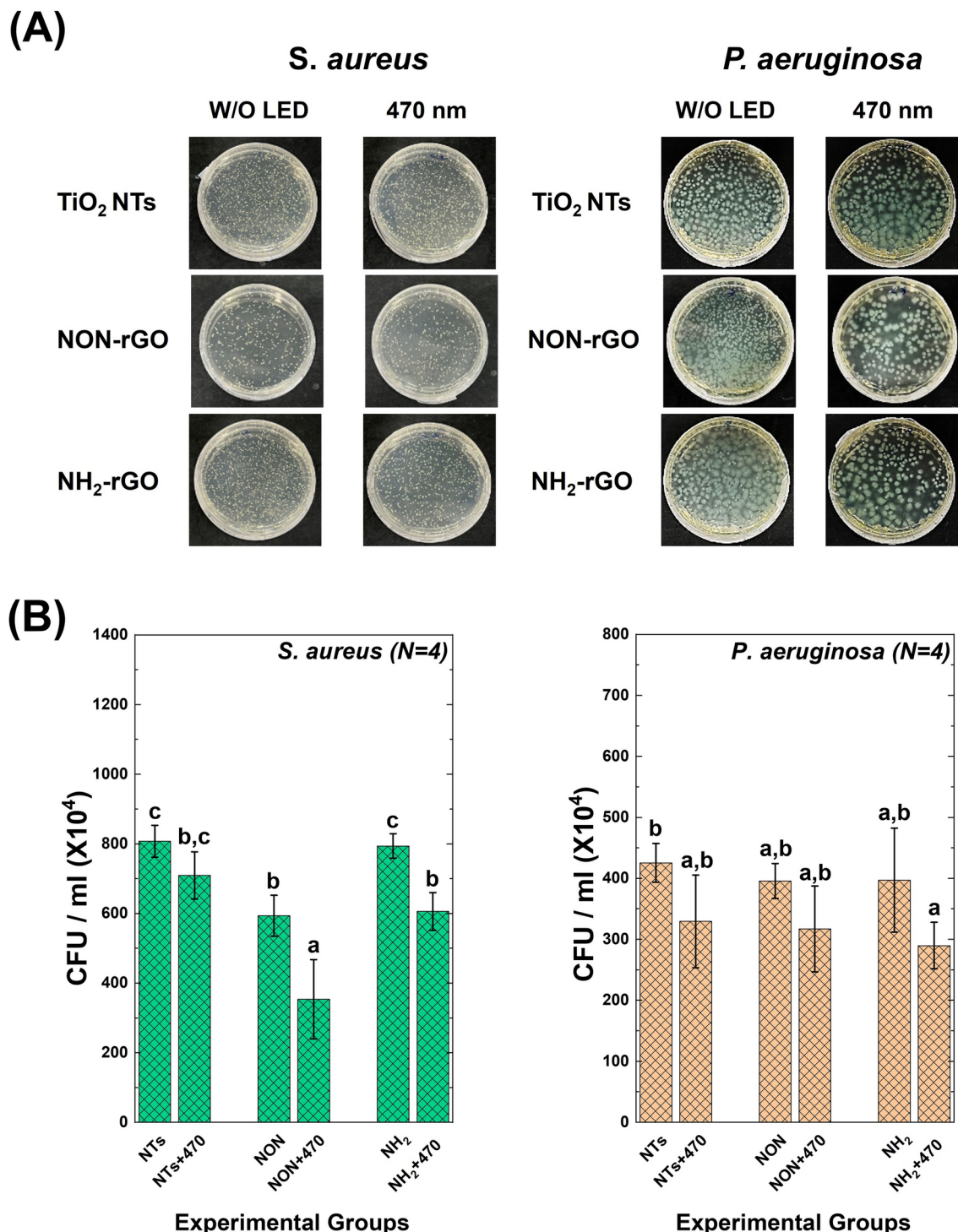


Fig. 8. (A) The photo images and (B) the results of CFU test of *S. aureus* and *P. aeruginosa* cultured on TiO₂ NTs, NON-rGO, and NH₂-rGO groups with 470 nm visible light irradiation (Different alphabetical letter means that there is significant difference between groups, $P < 0.05$).

we obtained the optical band gap of the experimental specimens by extrapolating the main line at a high energy level to the X-axis.

The PL spectra results show that lower PL spectral intensities were observed for the NON-rGO-TiO₂ NTs and NH₂-rGO-TiO₂ NTs groups than the results of the TiO₂ NTs control. Effective photocatalysts must be able to separate the charge carriers (electrons and holes) to facilitate redox reactions. The PL intensity measurements can reveal how well a material maintains these separated charge carriers. When a photocatalyst absorbs light, it generates electron–hole pairs; these charges need to be effectively separated and transported to the surface

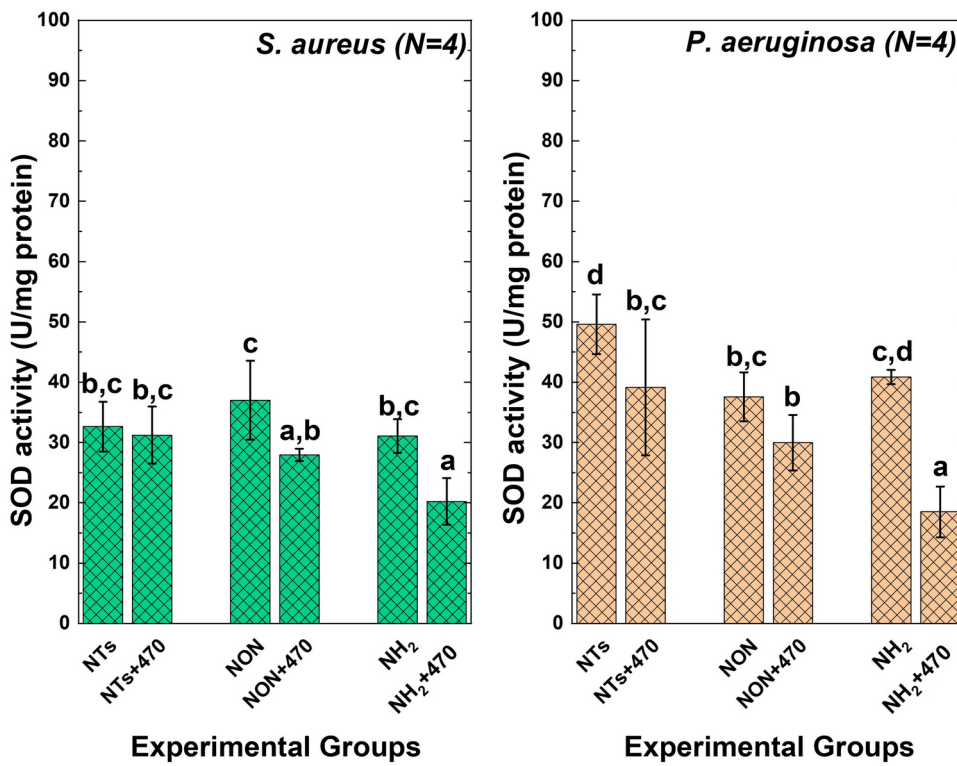


Fig. 9. Superoxide dismutase (SOD) enzyme activity of *S. aureus* and *P. aeruginosa* cultured on TiO₂ NTs, NON-rGO, and NH₂-rGO groups with 470 nm visible light irradiation (Different alphabetical letter means that there is significant difference between groups, *P*<0.05).

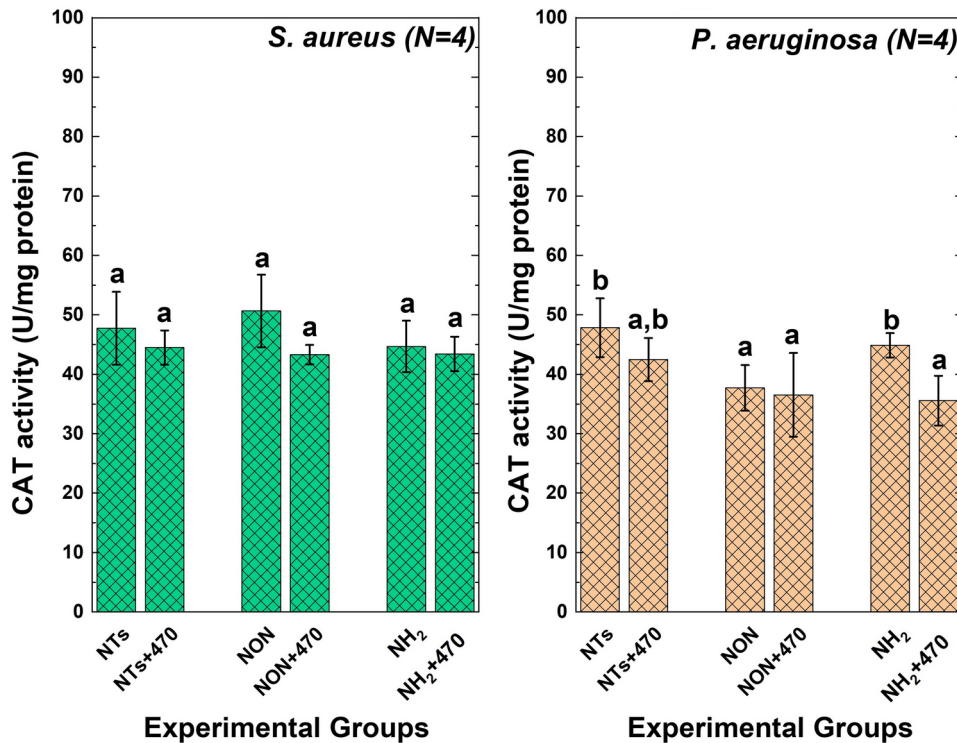


Fig. 10. Catalase (CAT) enzyme activity of *S. aureus* and *P. aeruginosa* cultured on TiO₂ NTs, NON-rGO, and NH₂-rGO groups with 470 nm visible light irradiation (Different alphabetical letters means that there is significant difference between groups, *P*<0.05).

of the material to participate in redox reactions. The phenomenon of PL arises from the recombination of excited electrons and holes. Therefore, a high PL intensity signifies a high rate of recombination, while a low PL intensity indicates that the charge carriers are efficiently separated and not readily recombining^{44,45}. Therefore, the results of PL spectra could be due to graphene acting as an electron transport material for TiO₂, limiting the recombination of e⁻ and h⁺. It can be concluded that graphene increased the photocatalytic activity efficiency of all the rGO-TiO₂ NTs composites under visible light.

The MTT assay results demonstrate that the group cell viability values were above 70%, regardless of visible light irradiation. However, the NON-rGO groups exhibited reduced cell viability after 48 h of incubation with and without visible-light irradiation. This decrease in cell viability in the non-rGO group was also observed in the live/dead stained images, and the number of cell attachments was lower than that in the NH₂-rGO and TiO₂ NTs groups, both with and without visible-light irradiation. In general, rGO is cytotoxic to cells, and the mechanisms of its toxicity have been described in many different ways, including interactions with cell membranes, reactive oxygen species, DNA damage, apoptosis, and autophagy, but remain incompletely understood^{46–48}. When the process of coating rGO onto TiO₂ NTs is considered, numerous factors such as the particle size, surface area, concentration, cell type, the degree of reduction (amount of remaining oxygen functional groups), and the presence of sharp edges are expected to determine its toxicity^{49–51}. Therefore, optimizing the coating time of rGO to achieve maximum photocatalytic effect with minimal thickness for good biocompatibility is the focus of this study. The optimal coating period of 1 min was selected, as it showed a uniform coating of rGO nanosheets and the best bandgap energy among all coating conditions (Figure S1, S2, and S3). The rGO nanosheets thinly and uniformly coated onto the TiO₂ NT surface exhibited excellent biocompatibility (Figure S4). In terms of the lower cell viability of the NON-rGO group, it is expected that the difference in surface energy as shown the results of contact angle measurement (Fig. 3) between the terminal functional groups of the rGO nanosheets was one of the main factors determining the initial attachment of cells, as shown by contact angle measurements. In addition, the NH₂-rGO group showed increased cell viability with increasing incubation period and visible light. The results of the live/dead and MTT assays performed in this study were insufficient for assessing the biological response of stem cells to the NH₂-rGO surface and the resulting osteogenic performance. Although further investigations are required to elucidate the reasons for the increase in the cell growth rate under visible light irradiation, within the limited conditions of this study, a time window of 1 min for coating of rGO exhibited the best photocatalytic effect and biocompatibility as illustrated in Figures S2, S3, and S4.

S. aureus and *P. aeruginosa*, representative gram-positive and gram-negative bacteria that cause a wide range of clinical diseases, are involved in biofilm formation and are associated with biomaterial-associated infections⁵². Therefore, these bacteria were selected for antibacterial testing. Based on the results of CFU antibacterial tests against *S. aureus* and *P. aeruginosa* and two enzyme activity tests (SOD and CAT), a reduction in the colony-forming ability of the two bacteria and inhibition of SOD/CAT enzyme activity were observed in the NH₂-rGO groups after visible light irradiation, except for the CAT enzyme activity against *S. aureus*. In general, rGO itself expresses antimicrobial activity by forming ROS through photocatalytic effects owing to its semiconductor properties, and it expresses a more substantial photocatalytic function under visible light irradiation in combination with TiO₂. To protect cells from toxic oxygen products, SOD catalyzes the formation of hydrogen peroxide from superoxide radicals, and CAT catalyzes the decomposition of hydrogen peroxide into water and oxygen^{48,49}. Therefore, although we were unable to identify a decrease in CAT enzyme activity against *S. aureus* within our limited experimental conditions, excess superoxide anions from the photocatalytic effect of aminated rGO-TiO₂ NTs attack the bacterial cell wall, resulting in the ability of SOD to scavenge superoxide anions and the ability of CAT to decompose hydrogen peroxide to decrease based on the overall results of the antimicrobial tests. Consequently, a reduction in SOD and CAT enzymatic activity results in the disruption of respiratory metabolism, leading to cell death.

The most common antimicrobial technologies that use light is UV light-based germicidal irradiation, wherein the DNA replication of bacteria is directly damaged, and this results in cell death⁵³. However, previous studies have reported that bacteria with multi-layered cell walls exhibit a stiffer and more rigid cell wall upon UV irradiation, but complete cell wall disruption and bacterial death were only observed with photocatalysis based on the combination of UV light and TiO₂⁵⁴. Photocatalysis based antimicrobial technologies exert their antimicrobial effects by generating ROS and super-hydroxyl ions from light irradiation to disrupt cell walls and inhibit the normal functionality of the bacteria. Therefore, practical antimicrobial effects can be predicted for surface-adherent bacteria, but are less effective for suspended planktonic bacteria. In addition, structural differences between gram-positive and gram-negative bacteria may cause changes to their antimicrobial effects based on their photocatalytic efficacy. In general, the bacterial cell wall is composed of peptidoglycans, and gram-negative bacteria have a single-layer cell wall. By contrast, gram-positive bacteria have multilayer cell walls.

Previous findings predicted that structural differences between gram-positive and gram-negative bacteria were the primary reason for the less effective antibacterial activity against *S. aureus* than against *P. aeruginosa*⁵⁵. However, the antimicrobial activities observed in the present study against both bacteria were excellent. This is because the combination of rGO and TiO₂ NTs, which individually express photocatalytic effects, showed enhanced antibacterial activity based on a more robust photocatalytic efficacy compared to previous studies.

On considering the clinical applications of this study in the field of dentistry, it has been observed that a combination of visible light and rGO-TiO₂ NTs has the potential for use in various dental prosthetic materials made of titanium such as implants, guided bone regeneration mesh, and orthodontic mini-screws^{56,57}. Additionally, visible light has a short penetration distance into the skin and cannot reach the deep areas of the implant body; however, it can readily penetrate the thin layer of the oral mucosa⁵⁸. Therefore, a combination of visible light and rGO-TiO₂ NTs is expected to be feasible for immediate antimicrobial treatment of the surgical site after dental surgery.

Overall, all antimicrobial activity evaluations comprehensively demonstrated that the bacteria used in this study exhibited a precise extinction mechanism influenced by the combination of visible light irradiation and aminated rGO-TiO₂ NT properties. Therefore, the combination of TiO NTs, with a high surface area and exceptional photocatalytic activity, and aminated rGO, with beneficial electronic properties and excellent biocompatibility, is expected to make the composite particularly effective for biomedical applications, including infection prevention in medical implants.

Conclusions

Within the limited range of bacterial strains and rGO types examined in this study, the combination of rGO-coated TiO₂ NTs and visible light demonstrated an excellent antimicrobial performance. Unlike previous studies that coated precious metal nanoparticles as stepping stones to help express the photocatalytic effect lacking under visible light, this approach leveraged the superior photocatalytic properties of each component, resulting in a more pronounced photocatalytic-based antimicrobial effect under visible light. Furthermore, the excellent biocompatibility of aminated rGO-coated TiO₂ NTs is anticipated to provide a foundation for developing novel surface treatment technologies for implantable devices, offering enhanced antimicrobial efficacy and osteogenic performance.

Data availability

All data generated and analyzed during this study are included in this published article and its supplementary information file.

Received: 2 January 2025; Accepted: 11 February 2025

Published online: 19 February 2025

References

- Kocher, S. P., Reche, A. & Paul, P. The etiology and management of dental implant failure: A review. *Cureus* **14**, e30455. <https://doi.org/10.7759/cureus.30455> (2022).
- Alasqah, M. N. Antimicrobial efficacy of photodynamic therapy on dental implant surfaces: A systematic review of in vitro studies. *Photodiagnos. Photodyn. Ther.* **25**, 349–353. <https://doi.org/10.1016/j.pdpt.2019.01.018> (2019).
- Rahnama-Hezavah, M. et al. How can imbalance in oral microbiota and immune response lead to dental implant problems?. *Int. J. Mol. Sci.* **24**, 17620. <https://doi.org/10.3390/ijms242417620> (2023).
- Insua, A., Galindo-Moreno, P., Miron, R. J., Wang, H. L. & Monje, A. Emerging factors affecting peri-implant bone metabolism. *Periodontol* **2000**(94), 27–78. <https://doi.org/10.1111/prd.12532> (2024).
- Sandulescu, M., Sirbu, V. D. & Popovici, I. A. Bacterial species associated with peri-implant disease-a literature review. *Germs* **13**, 352–361. <https://doi.org/10.18683/germs.2023.1405> (2023).
- Yu, Y. M. et al. Biomaterials science and surface engineering strategies for dental peri-implantitis management. *Mil. Med. Res.* **11**, 29. <https://doi.org/10.1186/s40779-024-00532-9> (2024).
- Duarte-Mata, D. I. & Salinas-Carmona, M. C. Antimicrobial peptides immune modulation role in intracellular bacterial infection. *Front. Immunol.* **14**, 1119574. <https://doi.org/10.3389/fimmu.2023.1119574> (2023).
- Schneider, J. et al. Understanding TiO₂ photocatalysis: Mechanisms and materials. *Chem. Rev.* **114**, 9919–9986. <https://doi.org/10.1021/cr5001892> (2014).
- Etacheri, V., Di Valentini, C., Schneider, J., Bahnenmann, D. & Pillai, S. C. Visible-light activation of TiO₂ photocatalysts: Advances in theory and experiments. *J. Photoch. Photobio. C* **25**, 1–29. <https://doi.org/10.1016/j.jphotochemrev.2015.08.003> (2015).
- Moon, K. S., Park, Y. B., Bae, J. M., Choi, E. J. & Oh, S. H. Visible light-mediated sustainable antibacterial activity and osteogenic functionality of Au and Pt multi-coated TiO₂ nanotubes. *Materials (Basel)* <https://doi.org/10.3390/ma14205976> (2021).
- Moon, K. S., Choi, E. J., Bae, J. M., Park, Y. B. & Oh, S. Visible light-enhanced antibacterial and osteogenic functionality of Au and Pt nanoparticles deposited on TiO₂ nanotubes. *Materials (Basel)* <https://doi.org/10.3390/ma13173721> (2020).
- Liu, W. & Speranza, G. Tuning the oxygen content of reduced graphene oxide and effects on its properties. *Ac Omega* **6**, 6195–6205. <https://doi.org/10.1021/acsomega.0c05578> (2021).
- Sha, M. S. et al. Photocatalytic degradation of organic dyes using reduced graphene oxide (rGO). *Sci. Rep.-UK* <https://doi.org/10.1038/s41598-024-53626-8> (2024).
- Siong, V. L. E., Tai, X. H., Lee, K. M., Juan, J. C. & Lai, C. W. Unveiling the enhanced photoelectrochemical and photocatalytic properties of reduced graphene oxide for photodegradation of methylene blue dye. *Rsc Adv.* **10**, 37905–37915. <https://doi.org/10.1039/d0ra06703b> (2020).
- Tiwary, S. K., Singh, M., Chavan, S. V. & Karim, A. Graphene oxide-based membranes for water desalination and purification. *NPJ 2D Mater. Appl.* <https://doi.org/10.1038/s41699-024-00462-z> (2024).
- Wang, Y., Li, S. S., Yang, H. Y. & Luo, J. Progress in the functional modification of graphene/graphene oxide: A review. *RSC Adv.* **10**, 15328–15345. <https://doi.org/10.1039/d0ra01068e> (2020).
- ISO 10993-5 Biological evaluation of medical devices-Part 5: Tests for in vitro cytotoxicity. ISO (2009).
- Liu, X., Feng, Q., Bachhuka, A. & Vasilev, K. Surface modification by allylamine plasma polymerization promotes osteogenic differentiation of human adipose-derived stem cells. *ACS Appl. Mater Interfaces* **6**, 9733–9741. <https://doi.org/10.1021/am502170s> (2014).
- Zhou, H., Zou, F., Koh, K. & Lee, J. Antibacterial activity of graphene-based nanomaterials. *Adv. Exp. Med. Biol.* **1351**, 233–250. https://doi.org/10.1007/978-981-16-4923-3_11 (2022).
- Sengupta, I. et al. Bactericidal effect of graphene oxide and reduced graphene oxide: Influence of shape of bacteria. *Colloid Interfac Sci.* **28**, 60–68. <https://doi.org/10.1016/j.colcom.2018.12.001> (2019).
- Yu, L., Wang, L., Sun, X. B. & Ye, D. Q. Enhanced photocatalytic activity of rGO/TiO₂ for the decomposition of formaldehyde under visible light irradiation. *J. Environ. Sci.* **73**, 138–146. <https://doi.org/10.1016/j.jes.2018.01.022> (2018).
- Wang, P. et al. Dye-sensitization-induced visible-light reduction of graphene oxide for the enhanced TiO₂ photocatalytic performance. *ACS Appl. Mater. Inter.* **5**, 2924–2929. <https://doi.org/10.1021/am4008566> (2013).
- Mohammadi, M., Roknabadi, M. R., Behdani, M. & Kompany, A. Enhancement of visible and UV light photocatalytic activity of rGO-TiO₂ nanocomposites: The effect of TiO₂/Graphene oxide weight ratio. *Ceram. Int.* **45**, 12625–12634. <https://doi.org/10.1016/j.ceramint.2019.02.129> (2019).
- Luan, X. N. et al. Electrophoretic deposition of reduced graphene oxide nanosheets on TiO₂ nanotube arrays for dye-sensitized solar cells. *Electrochim. Acta* **111**, 216–222. <https://doi.org/10.1016/j.electacta.2013.08.016> (2013).

25. Makula, P., Pacia, M. & Macyk, W. How to correctly determine the band gap energy of modified semiconductor photocatalysts based on UV-vis spectra. *J. Phys. Chem. Lett.* **9**, 6814–6817. <https://doi.org/10.1021/acs.jpclett.8b02892> (2018).
26. Méndez-Romero, U. A., Pérez-García, S. A., Xu, X. F., Wang, E. G. & Licea-Jiménez, L. Functionalized reduced graphene oxide with tunable band gap and good solubility in organic solvents. *Carbon* **146**, 491–502. <https://doi.org/10.1016/j.carbon.2019.02.023> (2019).
27. Zhang, J., Zhou, P., Liu, J. & Yu, J. New understanding of the difference of photocatalytic activity among anatase, rutile and brookite TiO_2 . *Phys. Chem. Chem. Phys.* **16**, 20382–20386. <https://doi.org/10.1039/c4cp02201g> (2014).
28. Rahme, L. G. et al. Common virulence factors for bacterial pathogenicity in plants and animals. *Science* **268**, 1899–1902. <https://doi.org/10.1126/science.7604262> (1995).
29. Zhang, L. L. et al. Antibacterial activity and mechanism of ginger extract against. *J. Appl. Microbiol.* **133**, 2642–2654. <https://doi.org/10.1111/jam.15733> (2022).
30. Ali, I., Kim, S. R., Park, K. & Kim, J. O. One-step electrochemical synthesis of graphene oxide- TiO_2 nanotubes for improved visible light activity. *Opt. Mater. Express* **7**, 1535–1546. <https://doi.org/10.1364/OME.7.001535> (2017).
31. Ramani, A., Desai, B., Dholakiya, B. Z. & Naveen, T. Recent advances in visible-light-mediated functionalization of olefins and alkynes using copper catalysts. *Chem. Commun.* **58**, 7850–7873. <https://doi.org/10.1039/d2cc01611g> (2022).
32. Banerjee, S. et al. New insights into the mechanism of visible light photocatalysis. *J. Phys. Chem. Lett.* **5**, 2543–2554. <https://doi.org/10.1021/jz501030x> (2014).
33. Padmanabhan, N. T. et al. Graphene coupled TiO_2 photocatalysts for environmental applications: A review. *Chemosphere* <https://doi.org/10.1016/j.chemosphere.2020.129506> (2021).
34. Ganguly, P., Byrne, C., Breen, A. & Pillai, S. C. Antimicrobial activity of photocatalysts: Fundamentals, mechanisms, kinetics and recent advances. *Appl. Catal. B-Environ.* **225**, 51–75. <https://doi.org/10.1016/j.apcatb.2017.11.018> (2018).
35. Juan, C. A., Perez de la Lastra, J. M., Plou, F. J. & Perez-Lebna, E. The chemistry of reactive oxygen species (ROS) revisited: Outlining their role in biological macromolecules (DNA, lipids and proteins) and induced pathologies. *Int. J. Mol. Sci.* <https://doi.org/10.3390/ijms22094642> (2021).
36. Chahrour, K. M., Yam, F. K., Lim, H. S. & Abdalrheem, R. Synthesis of anodic TiO_2 nanotube arrays annealed at 700°C for UV photodetector. *J. Phys. Conf. Ser.* **1535**, 012012. <https://doi.org/10.1088/1742-6596/1535/1/012012> (2020).
37. Rajoria, S., Vashishtha, M. & Sangal, V. K. Electrochemical treatment of electroplating wastewater using synthesized GO/ TiO_2 nanotube electrode. *Environ. Sci. Pollut. R.* **30**, 71226–71251. <https://doi.org/10.1007/s11356-023-27366-7> (2023).
38. Chahrour, K. M. et al. Controlled synthesis of vertically aligned honeycomb TiO nanotube arrays: Effect of high-temperature annealing on physical properties. *Appl. Phys. A-Mater.* <https://doi.org/10.1007/s00339-019-2707-5> (2019).
39. Fang, D., Luo, Z. P., Huang, K. L. & Lagoudas, D. C. Effect of heat treatment on morphology, crystalline structure and photocatalysis properties of TiO_2 nanotubes on Ti substrate and freestanding membrane. *Appl. Surf. Sci.* **257**, 6451–6461. <https://doi.org/10.1016/j.apsusc.2011.02.037> (2011).
40. Kumari, P. et al. Engineering Schottky-like and heterojunction materials for enhanced photocatalysis performance—a review. *Mater. Adv.* **3**, 2309–2323. <https://doi.org/10.1039/D1MA01062J> (2022).
41. Balapure, A., Ray Dutta, J. & Ganesan, R. Recent advances in semiconductor heterojunctions: A detailed review of the fundamentals of photocatalysis, charge transfer mechanism and materials. *RSC Appl. Interfaces* **1**, 43–69. <https://doi.org/10.1039/D3LF00126A> (2024).
42. Baerends, E. J., Gritsenko, O. V. & van Meer, R. The Kohn-Sham gap, the fundamental gap and the optical gap: The physical meaning of occupied and virtual Kohn-Sham orbital energies. *Phys. Chem. Chem. Phys.* **15**, 16408–16425. <https://doi.org/10.1039/C3CP52547C> (2013).
43. Jubu, P. R., Yam, F. K., Igba, V. M. & Beh, K. P. Tauc-plot scale and extrapolation effect on bandgap estimation from UV-vis-NIR data-a case study of $\beta\text{-Ga}_2\text{O}_3$. *J. Solid State Chem.* <https://doi.org/10.1016/j.jssc.2020.121576> (2020).
44. Li, B. et al. Optimizing charge carrier dynamics in photocatalysts for enhanced CO_2 photoreduction: Fundamental principles, advanced strategies, and characterization techniques. *Next Energy* **7**, 100222. <https://doi.org/10.1016/j.nxener.2024.100222> (2025).
45. Phanichphant, S., Nakaruk, A., Chansaenpak, K. & Channei, D. Evaluating the photocatalytic efficiency of the BiVO(4)/rGO photocatalyst. *Sci. Rep.* **9**, 16091. <https://doi.org/10.1038/s41598-019-52589-5> (2019).
46. Cebadero-Dominguez, O., Casas-Rodríguez, A., Puerto, M., Cameán, A. M. & Jos, A. Safety assessment of reduced graphene oxide in human monocytes and T cells. *Environ. Res.* <https://doi.org/10.1016/j.envres.2023.116356> (2023).
47. Kretowski, R. & Cechowska-Pasko, M. The reduced graphene oxide (rGO) Induces apoptosis, autophagy and cell cycle arrest in breast cancer cells. *Int. J. Mol. Sci.* <https://doi.org/10.3390/ijms23169285> (2022).
48. Lingaraju, K., Raja-Naika, H., Nagaraju, G. & Nagabushana, H. Biocompatible synthesis of reduced graphene oxide from *Euphorbia heterophylla* (L.) and their in-vitro cytotoxicity against human cancer cell lines. *Biotechnol. Rep. (Amst.)* **24**, 00376. <https://doi.org/10.1016/j.btre.2019.e00376> (2019).
49. Ahamed, M., Akhtar, M. J., Khan, M. A. M. & Alhadlaq, H. A. Reduced graphene oxide mitigates cadmium-induced cytotoxicity and oxidative stress in HepG2 cells. *Food Chem Toxicol* <https://doi.org/10.1016/j.fct.2020.111151> (2020).
50. Bellier, N., Baipaywad, P., Ryu, N., Lee, J. Y. & Park, H. Recent biomedical advancements in graphene oxide- and reduced graphene oxide-based nanocomposite nanocarriers. *Biomater. Res* <https://doi.org/10.1186/s40824-022-00313-2> (2022).
51. Ahmad, N. S., Abdullah, N. & Yasin, F. M. Toxicity assessment of reduced graphene oxide and titanium dioxide nanomaterials on gram-positive and gram-negative bacteria under normal laboratory lighting condition. *Toxicol. Rep.* **7**, 693–699. <https://doi.org/10.1016/j.toxrep.2020.04.015> (2020).
52. Mack, D. et al. Mechanisms of biofilm formation in *Staphylococcus epidermidis* and *Staphylococcus aureus*: functional molecules, regulatory circuits, and adaptive responses. *Int. J. Med. Microbiol.* **294**, 203–212. <https://doi.org/10.1016/j.ijmm.2004.06.015> (2004).
53. Bansaghi, S. & Klein, J. Evaluation of the antimicrobial effect of a far-uv radiation lamp in a real-life environment. *Infect. Prevent. Pract.* **6**, 100390. <https://doi.org/10.1016/j.infip.2024.100390> (2024).
54. Henderson, M. A. A surface science perspective on TiO_2 photocatalysis. *Surf. Sci. Rep.* **66**, 185–297. <https://doi.org/10.1016/j.surfrep.2011.01.001> (2011).
55. Moon, K. S., Bae, J. M., Oh, S. & Choi, E. J. Enhanced photocatalytic antibacterial activity of Au-coated Ni-Ti-O nanotubes for biomedical applications. *Mater. Chem. Phys.* <https://doi.org/10.1016/j.matchemphys.2024.128910> (2024).
56. Briguglio, F. et al. The use of titanium mesh in guided bone regeneration: A systematic review. *Int. J. Dent.* **2019**, 9065423. <https://doi.org/10.1155/2019/9065423> (2019).
57. Deguchi, T. et al. The use of small titanium screws for orthodontic anchorage. *J. Dent. Res.* **82**, 377–381. <https://doi.org/10.1177/154405910308200510> (2003).
58. Stasio, D. D. et al. Measurement of oral epithelial thickness by optical coherence tomography. *Diagnostics (Basel)* <https://doi.org/10.3390/diagnostics9030090> (2019).

Acknowledgements

This research was supported by the National Research Foundation of Korea (NRF), Grant Number 2022R1A2C1006565, funded by the Korean government (MSIT).

Author contributions

E.C. and S.O. conceived and designed most experiments, analyzed data, wrote the manuscript, and supervised the research; K.M. carried out experiments, collected data; J.B. conceptualization and reviewed and edited the manuscript. All authors reviewed and concurred with the submitted manuscript.

Declarations

Competing interests

The authors declare that they have no known competing financial interests or personal relationships that could have appeared to influence the work reported in this paper.

Additional information

Supplementary Information The online version contains supplementary material available at <https://doi.org/10.1038/s41598-025-90270-2>.

Correspondence and requests for materials should be addressed to S.O.

Reprints and permissions information is available at www.nature.com/reprints.

Publisher's note Springer Nature remains neutral with regard to jurisdictional claims in published maps and institutional affiliations.

Open Access This article is licensed under a Creative Commons Attribution-NonCommercial-NoDerivatives 4.0 International License, which permits any non-commercial use, sharing, distribution and reproduction in any medium or format, as long as you give appropriate credit to the original author(s) and the source, provide a link to the Creative Commons licence, and indicate if you modified the licensed material. You do not have permission under this licence to share adapted material derived from this article or parts of it. The images or other third party material in this article are included in the article's Creative Commons licence, unless indicated otherwise in a credit line to the material. If material is not included in the article's Creative Commons licence and your intended use is not permitted by statutory regulation or exceeds the permitted use, you will need to obtain permission directly from the copyright holder. To view a copy of this licence, visit <http://creativecommons.org/licenses/by-nc-nd/4.0/>.

© The Author(s) 2025